Nano Today 57 (2024) 102317

Contents lists available at ScienceDirect

Nano Today

journal homepage: www.elsevier.com/locate/nanotoday

Harnessing endocytic pH gradients for cascaded formation of intracellular condensates to inhibit autophagy: A pathway to cancer therapy

Jing Wang [a,b], Laicheng Zhou [b], Huaimin Wang [b,*]

[a] Department of Life Sciences, Fudan University, Shanghai 200433, China
[b] Department of Chemistry, School of Science, Westlake University, No. 600 Yungu Road, Hangzhou, Zhejiang 310030, China

ARTICLE INFO

Keywords:
Self-assembly
Peptide
Autophagy inhibition
Nanofiber
Lysosomal membrane permeability

ABSTRACT

Cancer cells rely on autophagy to degrade damaged organelles and survive in the harsh environment for progression and metastasis. Autophagy inhibition can improve the efficacy of anticancer therapy because many anticancer drugs can induce protective autophagy in cancer cells. However, current clinically available autophagy inhibitors are rare and have adverse effects with limited selectivity. This work develops an intracellular biomolecular condensate for autophagy inhibition to kill cancer without apparent side effects. A modularly designed amphiphilic peptide (PNP) can self-assemble to form toxic nanofibrous condensates successively from nanoparticles with the pH changes of the endocytic pathway. Mechanistic studies by CLSM and FRAP demonstrate that the PNP finally forms solid nanofibrous condensates in the lysosome after cell endocytosis. Bio-EM and cell transfection with adenovirus expressing mCherry-GFP-LC3B fusion protein (autophagy marker) experiments indicate the autophagy inhibition by PNP nanofibrous condensates. In vitro experiments show that PNP can significantly boost the activity of the clinical drug by 150-fold against drug-resistant lung cancer cells by inducing G2/M phase arrest of the cell cycle. Furthermore, PNPs demonstrate effective tumor targeting and permeability in vivo, inhibiting tumor growth and reducing the side effects of clinical chemotherapy drugs. Overall, this work provides a simple and feasible strategy for designing intracellular condensates to inhibit autophagy for cancer therapy.

Introduction

Since Christian de Duve coined the term in 1963, autophagy has garnered significant attention due to its potential implications for human health and disease, especially in cancers [1–6]. Autophagy is a fundamental catabolic process that engulfs cellular proteins or damaged organelles into double-membrane vesicles known as autophagosomes, which then fuse lysosomes to digest their contents [7,8]. Autophagy acts as a pro-survival mechanism in cancer cells, allowing them to adapt to the stressful conditions induced by anticancer drugs [9–12]. For example, some chemotherapeutic agents, such as taxanes and platinum-based drugs, could induce autophagy as a protective response of cancer cells, limiting their effectiveness [9,10]. Currently, chloroquine (CQ) and hydroxychloroquine (HCQ) are the only clinically available drugs to inhibit autophagy, which could increase the anti-cancer efficiency of chemotherapy or radiotherapy drugs by preventing the degradation of cargos [13–15]. Thus, developing a novel strategy for inhibiting autophagy is urgent and desirable.

Self-assembly, as a prevalent naturally occurring process, serves as a general strategy for designing and constructing functional therapeutics [16–22]. The developed 'in-situ self-assembly' to produce functional assemblies by synthetic organic molecules opens up a new avenue to create structures with specific biological functions in living cells [23–36]. Although significant advances have been achieved in the last two decades, utilizing in-situ self-assembly of amphiphilic peptides for inhibiting autophagy is rare and remains a challenge because of the complex environment of autophagy [37–40].

This work describes successive self-assembly of a pH-dependent modular amphiphilic peptide (PNP) with a morphology transformation following the processes of endocytosis (Scheme 1a). PNPs form uniform nanoparticles at pH 7.4, and as the pH decreases, they gradually self-assemble into nanofibers, forming a mixture of nanoparticles and nanofibers. Finally, the aggregates of nanofibers are formed when the pH drops to 4.5. These pH-dependent phase transitions synchronize with a series of maturation stages of endosomes, including early endosomes, late endosomes, and lysosomes. During the maturation

* Corresponding author.
E-mail address: wanghuaimin@westlake.edu.cn (H. Wang).

https://doi.org/10.1016/j.nantod.2024.102317
Received 14 March 2024; Received in revised form 30 April 2024; Accepted 16 May 2024
Available online 23 May 2024

of endosomes, the variation in pH plays a critical role in regulating cellular processes, and PNPs utilize this variation to achieve an antitumor effect through multiple mechanisms: (1) After endocytosis by cancer cells, the nanoparticles transform into nanofibers due to the pH variation within the endosome. The intra-lysosomal nanofibrous aggregates enhance the lysosomal membrane permeability(LMP), leading to the release of hydrolase and acidic contents into the cytoplasm, ultimately causing cell death; (2) Enhanced LMP facilitates the release of PNPs from lysosomes, and the overexpressed GSH in the cytoplasm breaks the disulfide bond to promote the disintegration of nanoparticles, resulting in controllable release of hydrophobic drugs; (3) Nanofibrous aggregates of PNPs could act as an autophagy inhibitor, and are capable of deacidifying lysosomes and inhibiting the degradation ability of autolysosomes, ultimately addressing drug resistance.

Results and discussion

Molecular design and characterization of condensates

To afford the successive self-assembly of molecules under the pH of the endocytic pathway [41], we employed a pH-responsive peptide vealyl (Val-Glu-Ala-Leu-Tyr-Leu, the lowercase letter indicates D-amino acid) [42], and modified it with tumor-targeting sequence RGD (Arg--Gly-Asp) at the C terminal of the peptide. We chose hydrophobic drugs (Paclitaxel or SN38) to balance the amphiphilicity of the peptide because not only they can provide intermolecular π-π stacking and hydrophobic interactions [29,43,44], but they can also serve as a suitable model for investigating autophagy inhibition since autophagy formation is one of the drug-resistant mechanism[2]. We also introduced a disulfide bond to conjugate the hydrophobic drug and peptide to achieve GSH-responsive drug release in the tumor microenvironment [35, 45–48].

We used solid-phase peptide synthesis (SPPS) with liquid chemical coupling to obtain **PTX-PNP** and **SN38-PNP** (Scheme S1-S2). Liquid chromatography-mass spectrometry (LC-MS) and nuclear magnetic resonance spectroscopy (^{1}H NMR) were introduced to verify the successful synthesis of these compounds (Figure S1-S10). To investigate the self-assembly properties of **PTX-PNP** at different pH conditions, transmission electron microscopy (TEM) was performed (Fig. 1a). **PTX-PNP** self-assembles into uniform nanoparticles with an average diameter of 8.1 nm at pH 7.4, consistent with the hydrodynamic diameter determined by dynamic light scattering (DLS) (Fig. 1b). The nanoparticles transformed into nanofibers with a decrease in pH value. The results show a mixture of nanoparticles and nanofibers at pH 6.5 and 5.5, respectively. Nanoparticles are entirely transformed into aggregates composed of nanofibers when the pH drops to 4.5. Besides, the turbidity assay shows that the absorption value of **PTX-PNP** at 600 nm gradually increased with the decrease in pH value, demonstrating the formation of bigger **PTX-PNP** aggregates (Fig. 1d). Since the stability of nanostructures in serum can influence the efficacy of therapeutic molecules [49,50], we next evaluated the *in vitro* stability of **PTX-PNP** in phosphate-buffered saline (PBS) buffer containing 10% fetal bovine serum (FBS) and F-12 K complete culture medium at 37°C by HPLC and DLS (Fig. 1c and Figure S13). These results indicate that the retention time and peak area of **PTX-PNP** remained unchanged, and we can hardly observe any new peaks. Furthermore, the particle sizes of **PTX-PNP**

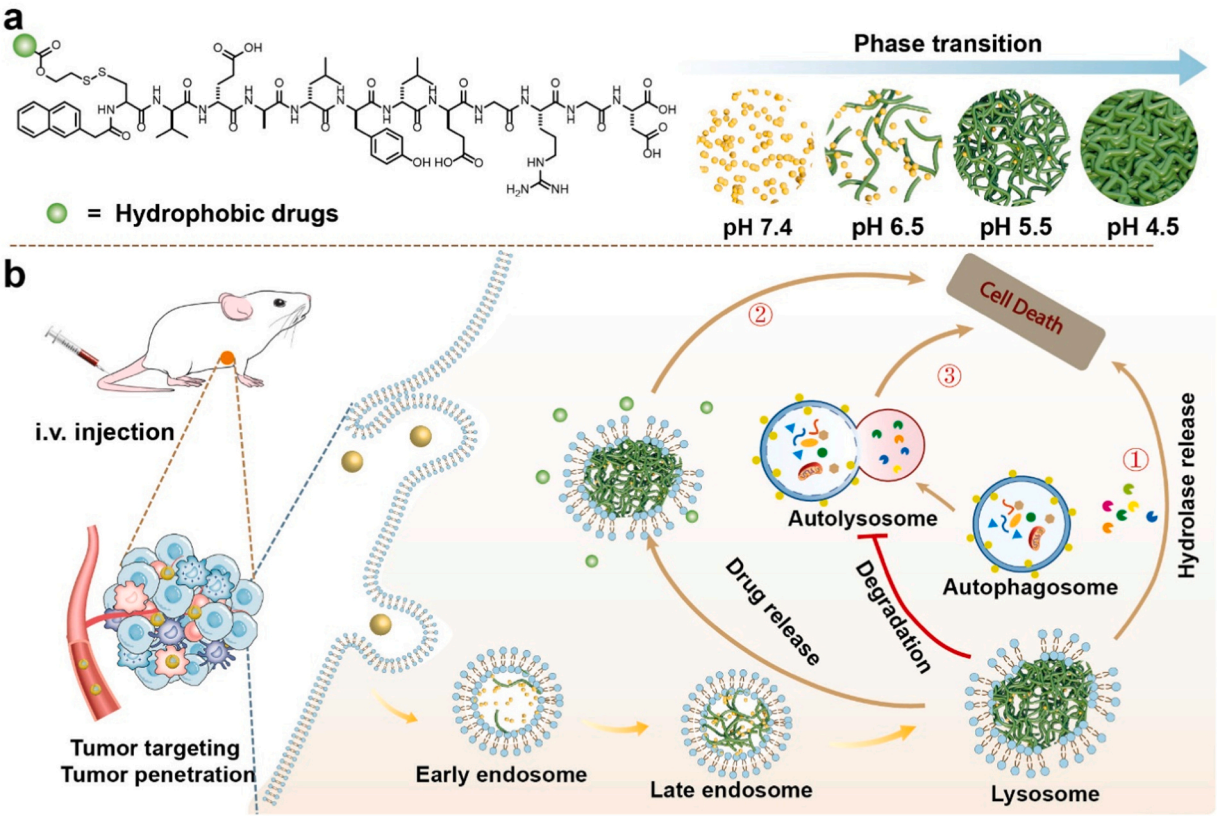

Scheme 1. Schematic illustration of the *in vitro* and *in vivo* antitumor effects of PNPs with the pH-dependent morphology transformation from nanoparticles to nanofibers. (a) Molecular structure of PNPs and the illustration of pH-dependent morphology transformation. (b) Schematic illustration of the nanostructure transformations of PNPs during cellular internalization and the multiple mechanisms of LMP-enhanced chemotherapy on cancer cells: (1) The intra-lysosomal nanofibrous aggregates induce the release of acidic contents and hydrolases into the cytoplasm, causing damage to the surrounding organelles and leading to cell death; (2) PNPs released from lysosomes are cleaved by the overexpressed GSH in the cytoplasm, promoting the release of drug to act on the target site; (3) Nanofibrous aggregates of PNPs deacidify lysosomes and inhibit the degradation ability of autolysosomes, acting as an autophagy inhibitor to prevent cancer cells from self-protection.

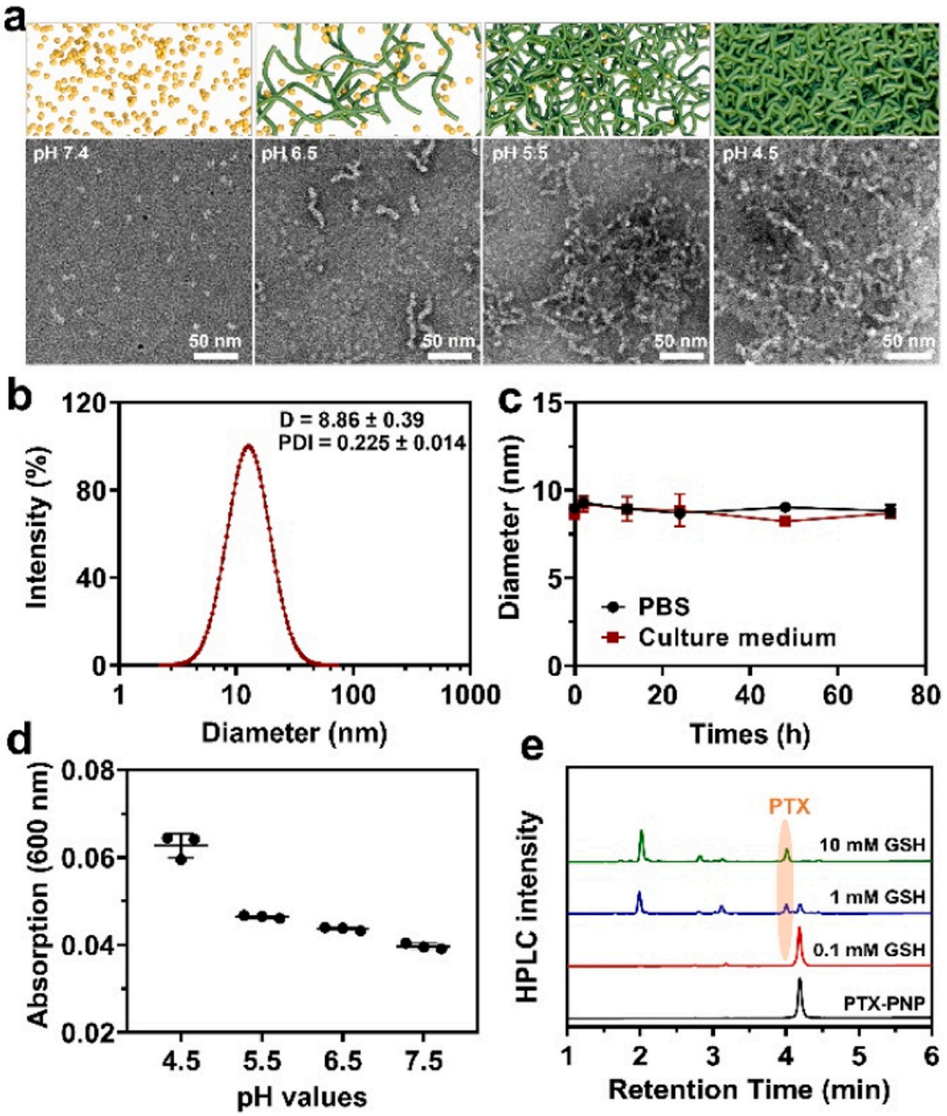

Fig. 1. The characterization of **PTX-PNP**. (a) TEM images of **PTX-PNP** (10 μM) in PBS buffer at pH 7.4, 6.5, 5.5, and 4.5. The scar bar is 50 nm. (b) The hydrodynamic diameter of **PTX-PNP**. (c) The hydrodynamic diameter variation of **PTX-PNP** incubated with a PBS buffer and an F-12 K complete culture medium. Data are presented as mean ± SD, n =3. (d) Turbidity assay of 10 μM **PTX-PNP** under different pH conditions. Data are presented as mean ± SD, n =3. (e) HPLC traces of 100 μM **PTX-PNP** incubated with PBS buffer containing 0.1 mM, 1 mM, and 10 mM GSH at 37°C for 48 h.

remained unchanged after incubating in FBS containing buffers for 72 h, demonstrating the stability of **PTX-PNP**. Besides, to assess the stability of **PTX-PNP** during *in vivo* administration, we co-incubated **PTX-PNP** with serum collected from mice at 37°C, and the stability was determined by HPLC (Figure S14). The results suggested that **PTX-PNP** was stable in serum after 24 h incubation, with a degradation rate of 9.4%. All these results demonstrate that **PTX-PNP** is stable both *in vitro* and *in vivo*.

To examine the responsive ability of **PTX-PNP** in the tumor reductive microenvironment, we used HPLC analyses (Fig. 1e and Figure S15) to test the components of the system in the presence of reduced glutathione (GSH) at different concentrations. The results show that PTX can be wholly released within 1 h at a high concentration of GSH (10 mM), while 1 mM GSH can induce 82% drug release from **PTX-PNP** after 48 h incubation. In contrast, **PTX-PNP** is much more stable in the presence of a low concentration of GSH (0.1 mM). These results suggest the tumor microenvironment specific controlling drug release because the concentration range of GSH within tumor cells is 1–10 mM[45,51,52]. These results together confirm that the self-assembly property of **PNP** can be governed by the gradually changing the system's pH value, and the reductive environment in the cytoplasm could control the release of the drug from PNPs after escaping from the lysosome. **SN38-PNP** also exhibited the nanoparticles-aggregates transition and GSH-responsive properties, confirming the broad applicability of PNPs (Figure S23).

Mechanistic studies of cellular uptake of PNPs and the corresponding self-assembly properties in cells

We synthesized a fluorophore-labeled PNP (**PTX-fPNP**) by replacing the N-terminal naphthalene with nitrobenzofurazan (NBD)[53] (Scheme S3 and Figure S11) to directly visualize the cellular distribution of PNP and the intracellular assembly behaviors in living cells. The modification of NBD maintains the pH-dependent self-assembly behaviors and undergoes morphological transformation under different pH conditions (Figure S16). We utilized endocytic inhibitors to co-incubate with peptides to examine whether **PTX-fPNP** distributes in lysosomes through the endocytic pathway (Fig. 2a and b). The results indicate that adding filipin (an inhibitor of caveolae-mediated endocytosis) reduced the uptake of **PTX-fPNP** by about 33%. Two other inhibitors, chlorpromazine (an inhibitor of clathrin-mediated endocytosis) and EIPA (an inhibitor of

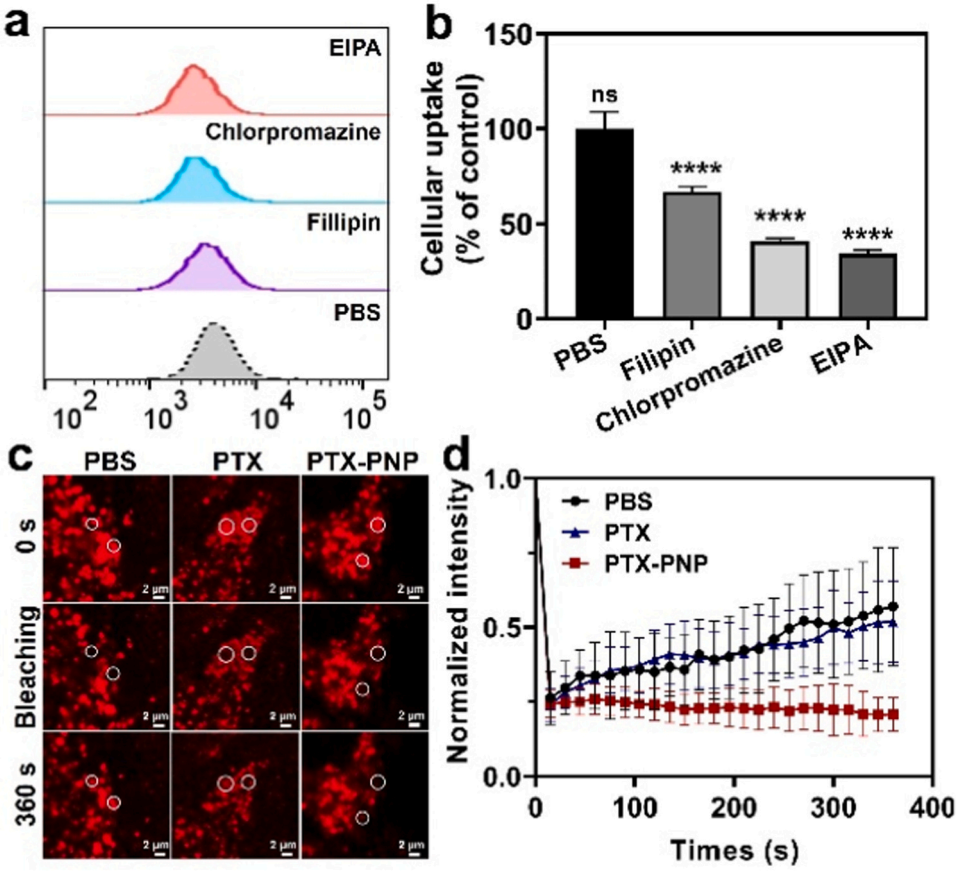

Fig. 2. Mechanistic studies of cellular uptake of **PTX-PNP** and their intra-lysosomal self-assembly property. (a) Effect of endocytosis inhibitors (Filipin 3 μM, Chlorpromazine 15 μM, EIPA 25 μM) on the cellular uptake of **PTX-fPNP** determined by flow cytometry. (b) The percentage of intracellular fluorescence intensity of **PTX-fPNP** after treating different endocytosis inhibitors. Data are presented as mean ± SD, n =3, ns means no significance, ****p<0.0001, one-way ANOVA. (c) Fluorescence recovery after photobleaching (FRAP) images of lysosome sections in PTX or **PTX-PNP** (10 μM) treating A549 cells. Lysosomes are stained by LysoTracker Red and labeled as red signals. Scar bar is 2 μm. (d) FRAP recovery curves of lysosome sections in PTX or **PTX-PNP** treated cells (n = 14).

macropinocytosis), resulted in a 59% and 66% reduction in cellular uptake of **PTX-fPNP**. We also chose other three inhibitors and found that amiloride (inhibitor of macropinocytosis) and monodansylcadaverine (MDC, inhibitor of clathrin-mediated endocytosis) resulted in 38% and 19% reduction in cellular uptake of **PTX-fPNP**. While methyl--β-cyclodextrin (MβCD), an inhibitor of caveolae-mediated endocytosis, shows only a 10% reduction in cellular uptake of **PTX-fPNP** (Figure S17). These results suggested that the nanoparticles formed by **PTX-PNP** mainly undergo clathrin-mediated endocytosis and macropinocytosis pathways, which ensure the further accumulation of **PTX-PNP** in endosomes and ultimately refuse with lysosomes through pH variation during the endocytic process.

To investigate the self-assembly behaviors of PNPs in the lysosomes, we conducted fluorescence recovery after photobleaching (FRAP) experiments by bleaching the fluorescence signals of Lysotracker Deep Red (DND-99), which is a non-fixable fluorescent dye that stains acidic compartments within a cell. DND-99 can diffuse back into the photobleaching areas in the liquid phase, whereas it cannot diffuse or diffuse very slowly in the aggregated phase, resulting in poor fluorescence recovery. The results (Fig. 2c and d) show that the PBS and PTX-treated groups showed a strong fluorescence recovery, with the ability to recover from 25% to 57% and 52%, respectively. In contrast, the **PTX-PNP** treated group exhibits no fluorescence recovery, suggesting that **PTX-PNP** can form solid-like aggregates within lysosomes, providing a potential strategy for enhancing lysosomal permeability.

PNPs induce lysosomal membrane permeability (LMP)

Next, we evaluated the influence of **PTX-PNP** on LMP by determining the leakage of acridine orange (AO) into the cytoplasm. AO can be used as a dye to assess lysosomal integrity[54]. AO accumulates in the lysosomes and emits red fluorescence due to the acidic environment. Meanwhile, in the context of LMP, the integrity of the lysosomal membrane is disrupted, causing AO to leak into the cytoplasm and emit green fluorescence. Compared to the control and PTX-treated groups, the results (Figs. 3a, and 3b) show that there is a noticeable increase in green fluorescence in the cytoplasm in the **PTX-PNP** treated group, indicating the change of the lysosomal membrane integrity and the leakage of AO from lysosomes to the cytoplasm.

Time-dependent cellular uptake experiments by CLSM indicate that the aggregates of **PTX-PNP** could facilitate its escape from lysosomes by enhancing LMP (Fig. 3c). The green fluorescence from **PTX-PNP** colocalized with the red fluorescence from lysosomes (Fig. 3d) at the first 2 h incubation, indicating that **PTX-PNP** predominantly localized in the lysosomes. With the increase of incubation time, we can observe a noticeable formation of aggregates both inside and outside of lysosomes, and the fluorescent colocalization curves also confirmed that **PTX-PNP** enabled lysosomal escape (Fig. 3e). This phenomenon was also observed in **SN38-PNP** treated cells (Figure S24), indicating that this modular design can be used for a wide range of hydrophobic chemotherapeutic drugs.

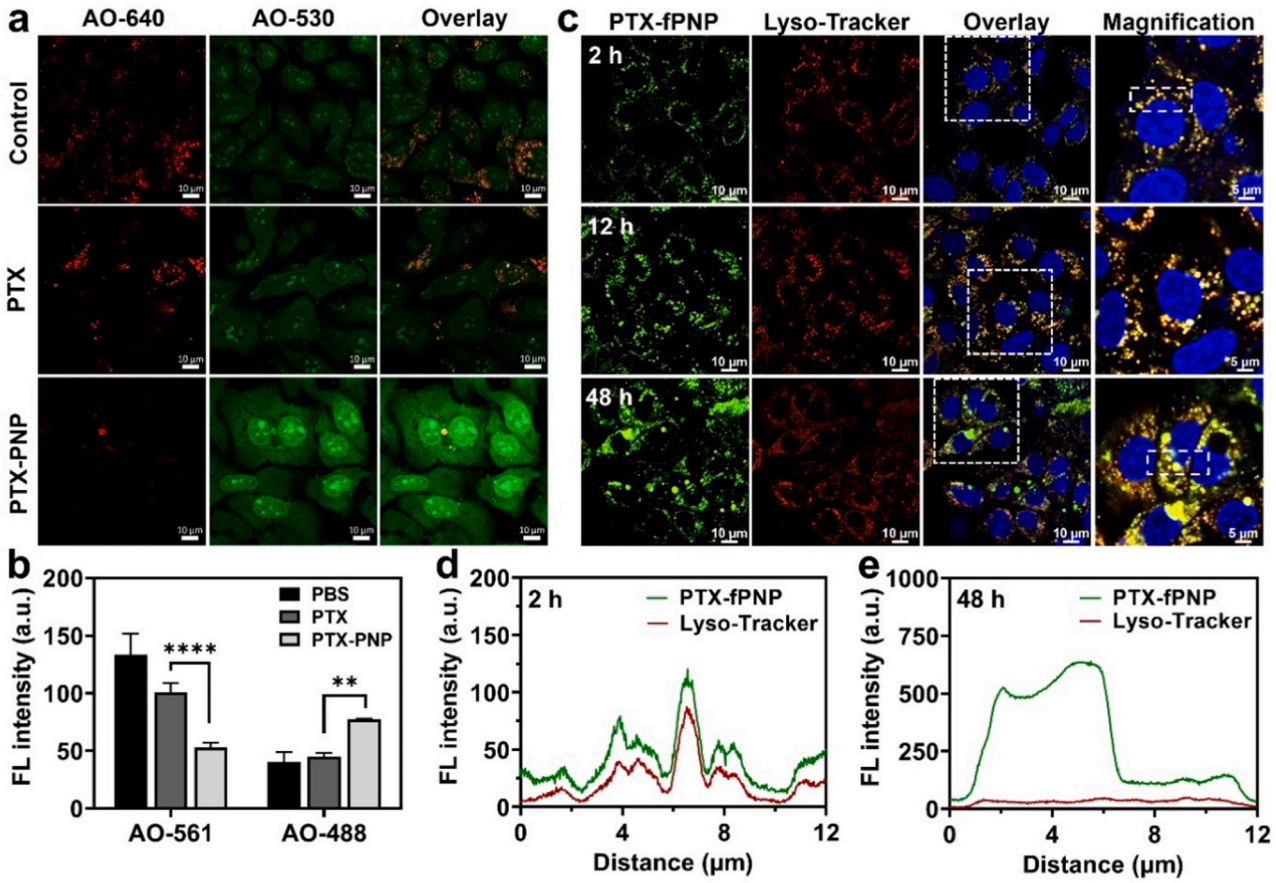

Fig. 3. In vitro Intracellular aggregates of **PTX-PNP** induce lysosomal membrane permeability. (a) Confocal laser scanning microscopy (CLSM) images of A549 cells treated with 5 μM Acridine Orange (AO) after the incubation of 10 μM PTX or **PTX-PNP** for 12 h. (b) Calculated mean AO fluorescence intensity of a. Data are presented as mean ± SD, n =3, **p < 0.01, ****p < 0.0001, two-way ANOVA. (c) Time-dependent CLSM images of A549 cells treated with 10 μM **PTX-fPNP** (green signals) at different times, and then lysosomes are stained with Lyso-Tracker (red signals). Scar bars are 10 μm in low-magnification images and 5 μm in high-magnification images. Co-localization profiles of **PTX-fPNP** and lysosome at 2 h (d) and 48 h (e).

The bioactivity of PTX-PNP against tumor cells

To examine whether **PTX-PNP** affects the cellular microtubule structure and microtubule-dependent processes, we used lung cancer cell line A549 and its corresponding paclitaxel-resistant cell line A549/Tax to conduct an immunofluorescence experiment. The results show that the microtubule structures in A549 cells (Fig. 4a) are disrupted, and multipolar spindles appeared in both PTX and **PTX-PNP**-treated cells, indicating the capability of causing mitotic arrest. In contrast, only **PTX-PNP** could induce the formation of multipolar spindles in paclitaxel-resistant cells A549/Tax. Cell cycle analysis results confirmed that **PTX-PNP** can induce G2/M phase arrest in A549 cancer cells and drug-resistant A549/Tax cancer cells. At the same time, PTX showed no significant effect on the cell cycle of A549/Tax cells (Figure S18), consistent with the clinical outcomes of cancer therapy, as the intratumoral drug concentrations in patients are too low to reach the effective concentration for mitotic arrest.

The cytotoxicity results indicated that **PTX-PNP** exhibited a better growth inhibitory effect on cancer cells than PTX (Fig. 4b and c). For A549 cells, the IC_{50} is 60.0 nM for **PTX** and 15.3 nM for **PTX-PNP** at 72 h treatment, while for A549/Tax cells, the IC_{50} is 109.0 μM for **PTX** and 0.7 μM for **PTX-PNP** at 72 h, demonstrating the superiority of **PTX-PNP** against drug-resistant cancer cells. Apoptosis/necrosis assay by flow cytometry indicated that PTX and **PTX-PNP** induced cell necrosis of 5.2% and 13.0% after 12 h treatment, 15.9% and 25.9% after 24 h of treatment, respectively (Fig. 4d and e), which are consistent with the abovementioned growth inhibition experiments, suggesting that **PTX-PNP** exhibited a better therapeutic effect compared to PTX.

The association between lysosomal defects induced by PTX-PNP and autophagy

To further explore the effects of **PTX-PNP** on lysosomes, we utilized biological electron microscopy (Bio-EM) to visualize the organelles after PNPs treatment (Fig. 5a and Figure S25). After damaging by chemotherapeutic drugs, cells could generate autophagy to clean up the damaged organelles and achieve self-protection[55,56]. Bio-EM results showed obvious degradative autolysosomes in cells treated with PTX for 24 h, indicating that they are in the process of autophagy. In contrast, cells treated with **PTX-PNP** for 6 h exhibited lysosomal membrane defects and leakages (labeled by black arrows). After 24 h treatment of **PTX-PNP**, we observed the accumulation of multilamellar bodies (MLBs), the typical characteristics of lysosomal storage diseases, such as the Niemann-Pick disease[57–61]. In these diseases, the deficiency of lysosomes prevents the clearance of macromolecular substrates, leading to the accumulation of autophagosomes, endolysosomes, and multilamellar bodies. Therefore, the accumulation of MLBs suggested that **PTX-PNP** caused lysosomal defects.

To further examine the relationship between lysosomal defects induced by **PTX-PNP** and autophagy, we transfected A549 cells with adenovirus expressing mCherry-GFP-LC3B fusion protein (AdPlus-mCherry-GFP-LC3B) to detect autophagy. Microtubule-associated protein 1 light chain 3B (LC3B) is a typical autophagy marker that undergoes post-translational modification during autophagosome

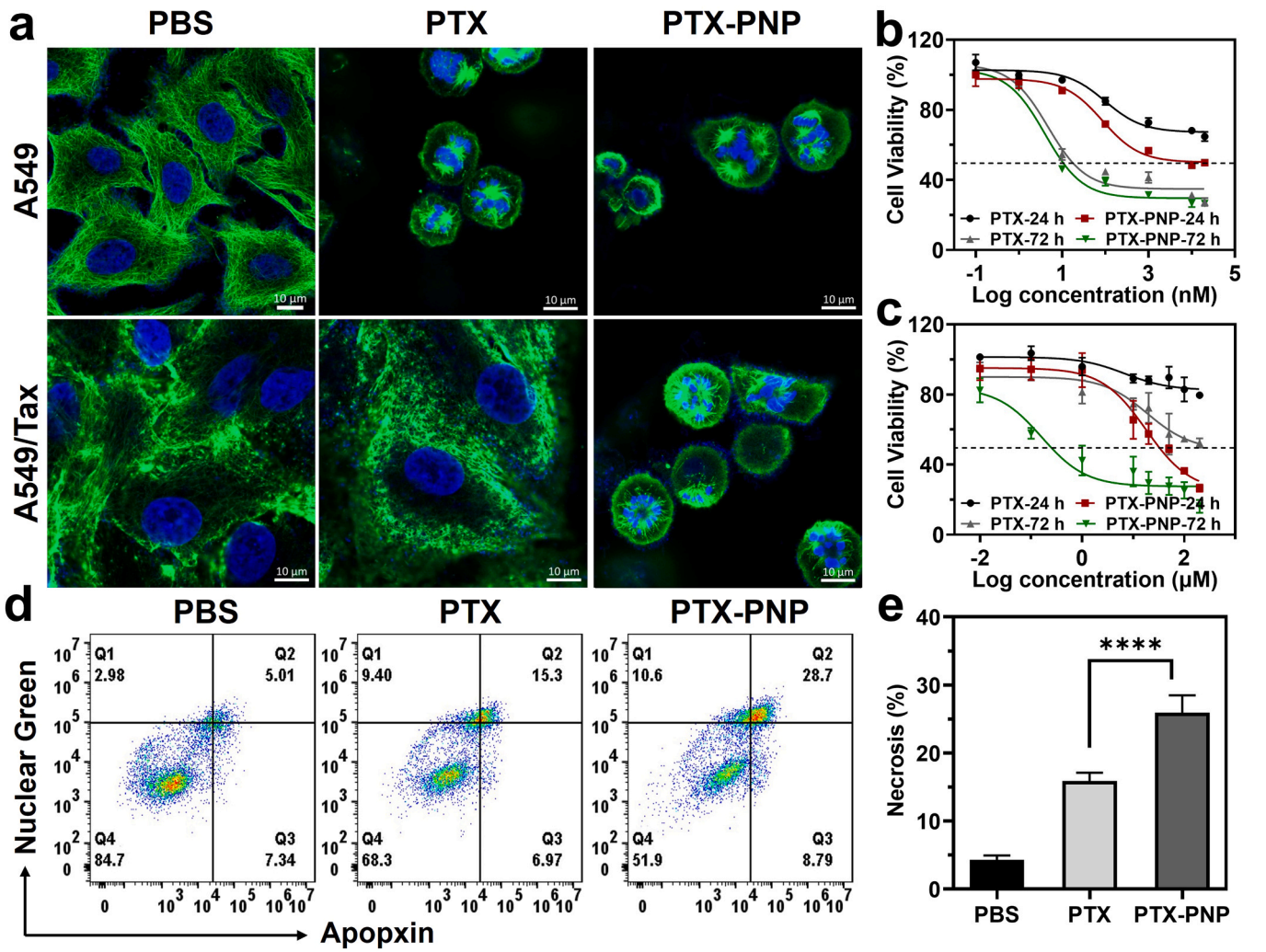

Fig. 4. Inhibitory effects of **PTX-PNP** on the cell viability, apoptosis/necrosis. (a) CLSM images of A549 cells and drug-resistance A549/Tax cells stained with α-tubulin antibody after treatment with 10 μM PTX or **PTX-PNP** for 24 h. (b) Cell viability of A549 cells treated with PTX or **PTX-PNP** for 24 and 72 h. (c) Cell viability of A549/Tax cells treated with PTX or **PTX-PNP** for 24 and 72 h. (d) Apoptosis and necrosis analysis of A549 cells treated with 10 μM PTX or **PTX-PNP** for 24 h. (e) Quantified necrosis of A549 cells of each treatment. Data are presented as mean ± SD, n =3, ***p < 0.001, ****p < 0.0001, one-way ANOVA.

formation. Cells transfected with adenovirus could express red fluorescent protein mCherry and green fluorescent protein GFP. During the fusion of autophagosome and lysosome, the acidic environment inside the lysosome will quench the GFP fluorescence and only emit the mCherry fluorescence, which is used to distinguish autophagosome and autolysosome. CLSM results (Fig. 5b) showed that the PTX-treated cells generated red puncta (mCherry+/GFP-), indicating the formation of autolysosomes. In contrast, red and green fluorescence signals (yellow puncta) could be observed in the **PTX-PNP** treated group, suggesting that PNP could elevate the internal pH of lysosomes, thereby inhibiting the fusion and degradation of autolysosomes, consistent with the positive group of HCQ treated cells. In addition, immunoblotting results also indicated that the expression of LC3B II was upregulated after the incubation with **PTX-PNP** and HCQ, demonstrating the inhibition of LC3B II degradation by autolysosome (Figs. 5c and 5d).

In vivo distribution of PNPs in the tumor-bearing mice

We next evaluated the tumor accumulation and retention ability of the compounds in A549 tumor-bearing NPSG mice. A widely used fluorescent probe, Cy5.5, is used to label peptides (**Cy5.5-PNP**) to investigate the in vivo distribution of PNPs (Figure S12). The **Cy5.5-PNP** can also form nanoparticles with a diameter of 10 nm at pH 7.4 and assemble into nanofibers at pH 4.5, demonstrating its capability to undergo a morphological transformation as the pH decreases (Figure S16). The mice were randomly divided into two groups when the tumor volume reached 200 mm^3, and then free Cy5.5 or **Cy5.5-PNP** were intravenously injected via the tail vein at an identical Cy5.5 dose of 3 mg/kg. Whole animal imaging revealed that free Cy5.5 exhibited a weak fluorescent signal at the tumor site, whereas **Cy5.5-PNP** generated a strong fluorescent signal at the tumor site at 4 h post-injection. After 96 h of injection, the tumor site still showed a strong fluorescent signal (Fig. 6a) after the treatment of **Cy5.5-PNP**. The ex vivo fluorescent results indicated that the fluorescent intensity of **Cy5.5-PNP** at the tumor site is much higher than that of Cy5.5, with a 4.2-fold increase (Figure S20) after post-injection for 8 h.

The tumor accumulation capability of PNPs was further validated by quantitatively measuring the drug concentration in organs and tumor sections by HPLC and LC-MS, respectively. The procedure for detecting the drug concentration is depicted in Fig. 6b. The intratumoral concentration of PTX in the **PTX-PNP** treated group is 6.7-fold higher than that of the PTX-treated mice (Fig. 6c). Using another hydrophobic drug, SN38, to replace PTX exhibits similar results (Fig. 6d), demonstrating the generality of this strategy.

The tumor permeability of PNPs was examined by CLSM imaging of the tumor sections. After i.v. Injection of Cy5.5 or **Cy5.5-PNP** for 8 h,

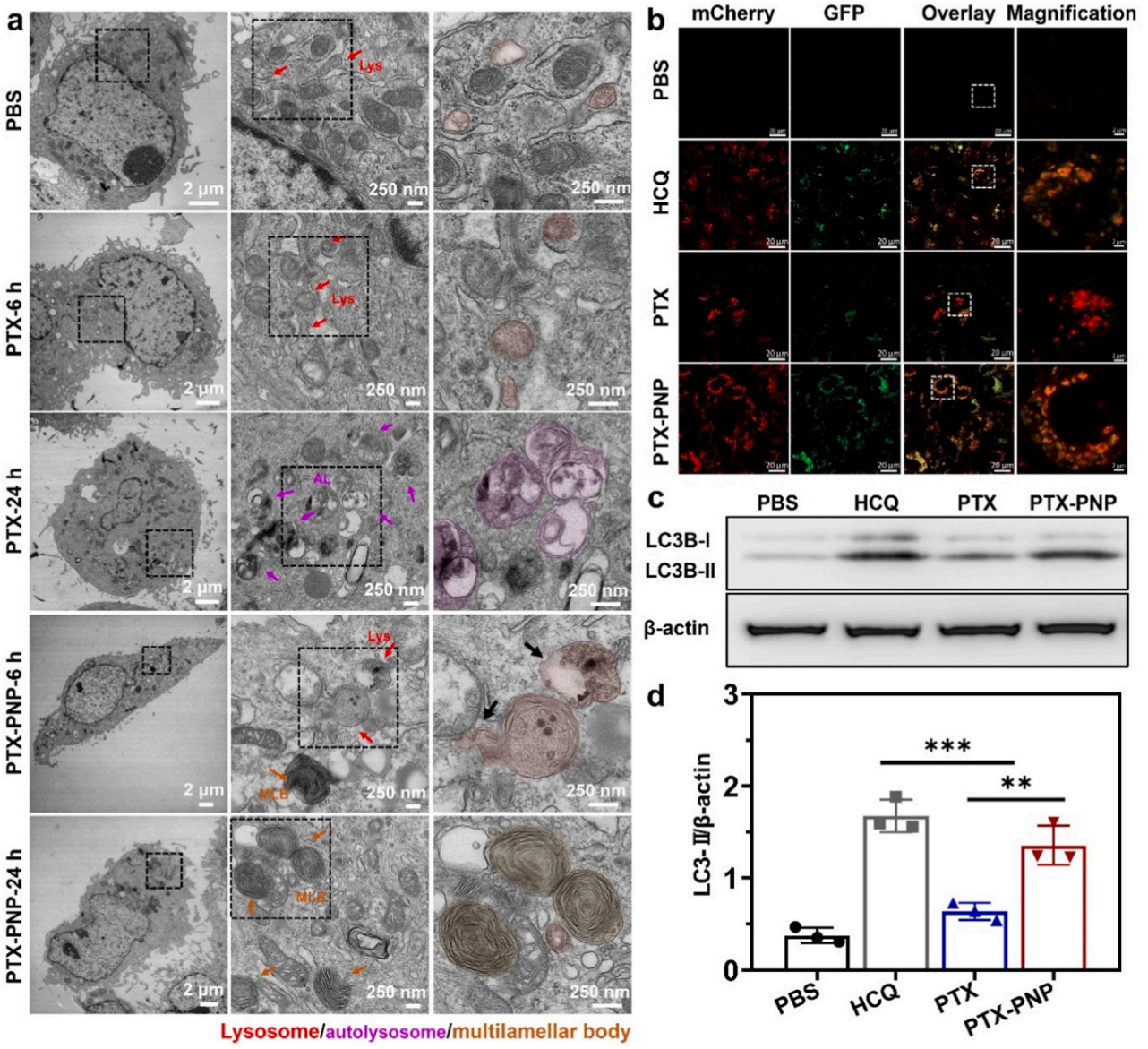

Fig. 5. The association between lysosomal defects induced by **PTX-PNP** and autophagy. (a) Bio-EM images of A549 cells treated with 10 μM PTX or **PTX-PNP** for 6 and 24 h; black arrows indicate the breakage of lysosomes; red/purple/orange arrows and areas indicated lysosomes/autolysosomes/multilamellar bodies. (b) CLSM images of A549 cells transfected with AdPlus-mCherry-GFP-LC3B that were treated with 10 μM HCQ, PTX, and **PTX-PNP** for 24 h. (c) Western blot results of LC3B in A549 cells after treatment with 10 μM HCQ, PTX, and **PTX-PNP** for 24 h. (d) Statistical data of the expression of autophagy indicator LC3B protein. Data are presented as mean ± SD, n = 3, n = 3, $^{**}p < 0.01$, $^{***}p < 0.001$, one-way ANOVA.

mice were euthanized, and tumor sections were dissected for immunofluorescent staining of CD31 and α-SMA. As shown in Fig. 6e, the red fluorescence from Cy5.5 in the Cy5.5 treated group mainly overlapped with the green fluorescent signals of CD31, indicating that Cy5.5 was primarily entrapped in the perivascular areas of the tumor. In contrast, **Cy5.5-PNP** penetrates through the tumor vessels and highly diffuses throughout the tumor mass, indicating the ability of **Cy5.5-PNP** to achieve intertumoral penetration. The co-localization profiles also demonstrated the tumor permeability of **Cy5.5-PNP** from the tumor vasculature (Fig. 6f and g).

Antitumor effects of PNPs in vivo

The antitumor efficacy of PNPs was evaluated in an A549 tumor mouse model. The tumor-bearing NPSG mice were randomly divided into five groups (n = 6) after the tumor volume reached 100 mm^3. Compounds were i.v. injected every 3 days at a PTX or SN38 dose of 10 mg/kg. The tumor volumes and body weight of mice were monitored every other day for 20 days (Fig. 7a). The tumor growth results indicated that chemotherapeutic drugs PTX and SN38 showed moderate antitumor efficacy compared with the saline group. Comparatively, **PTX-PNP** and **SN38-PNP** achieved significant antitumor efficacy (Fig. 7b). Furthermore, the dissected tumor mass at the end of the treatments suggested the elevated antitumor efficacy of PNPs, in which the tumor inhibition rate of **PTX-PNP** and **SN38-PNP** were 2.1- and 1.8-fold higher than that of PTX and SN38 (Fig. 7c), respectively. H&E and TUNEL staining assays further showed that the PNPs can partially induce the apoptosis of tumor cells (Fig. 7d). There was little change in the body weight of the treated mice during the antitumor study, except for an 8.5% weight loss in SN38-treated mice (Figure S21).

The organs were harvested for histological analysis to investigate the biosafety of PNPs. The H&E images of liver tissues in the PTX and SN38-treated groups showed that the cytoplasm of hepatocytes became vacuolated, and many apoptotic cells were distributed in the liver

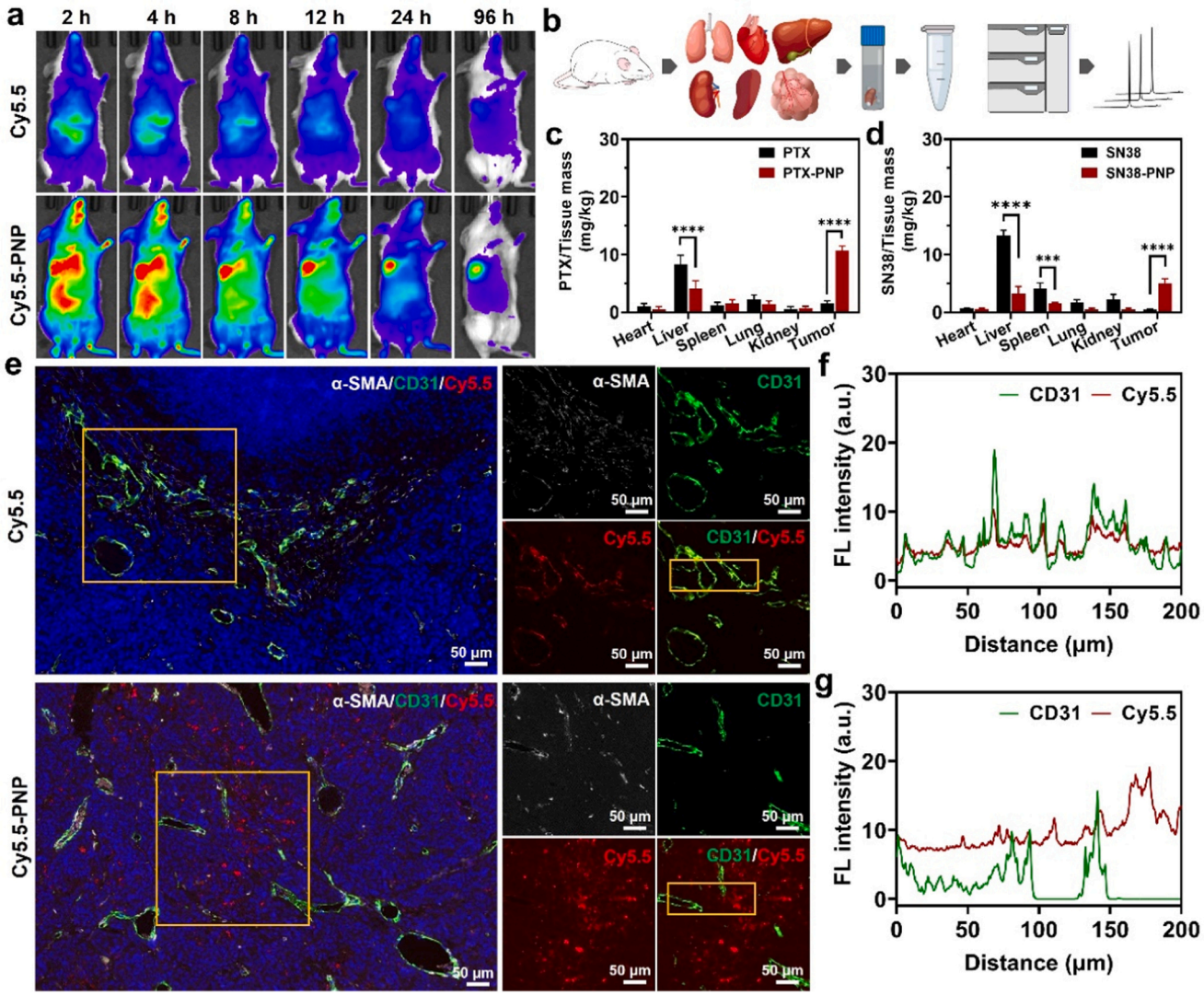

Fig. 6. In vivo distribution of PNPs in A549 tumor-bearing mice after treatments. (a) In vivo fluorescence images of A549 tumor-bearing mice at different time points after administering free Cy5.5 or **Cy5.5-PNP**. (b) Schematic diagram of the experimental procedure for determining the ex vivo distribution by HPLC. (c) Quantified PTX and (d) SN38 concentrations in organs and tumor sites determined by HPLC. Data are presented as mean ± SD, n = 3, $^{**}p < 0.01$, $^{***}p < 0.001$, $^{****}p < 0.0001$, one-way ANOVA. (e) CLSM images of inner tumor sections after 8 h post administration of free Cy5.5 or **Cy5.5-PNP** and immune-stained with anti-CD31 antibody (green), and anti-α-SMA antibody (white). Scar bars are 50 μm. Co-localization profiles of CD31 and Cy5.5 signals in (f) Cy5.5-treated and (g) **Cy5.5-PNP**-treated groups.

tissues. In contrast, no apparent apoptotic cells were observed in the liver tissues of the **PTX-PNP**, **SN38-PNP**, and saline-treated groups (Fig. 7e and g). In addition, PTX and SN38 caused an abnormal increase in the number of megakaryocytes in spleen tissues, suggesting that PTX and SN38 caused myelosuppression, the most common adverse reaction of chemotherapy. In contrast, no megakaryocyte was observed in the spleen of **PTX-PNP** or **SN38-PNP** treated groups (Fig. 7f and h). No significant damage was observed in other tissues (Figure S22). Taken together, the PNPs could achieve antitumor effects with negligible side effects through lysosome-dependent cell death and autophagy blockage.

Conclusion

In summary, this work reported a modular design of self-assembly amphiphilic peptides for autophagy inhibition to kill cancer without apparent side effects. The intracellular self-assembly morphologies of PNP respond to the pH changes of endocytic pathways. The finally formed nanofibrous condensates in the lysosome can induce LMP. The destruction of lysosomes further hinders the self-protective pathway of cancer cells by autophagy inhibition and addresses the drug resistance of cancer cells. Mechanistic studies used various techniques suggested that the autophagy inhibition plays a vital role in killing cancer. Experimental experiments at the cell level and in tumor-bearing mice demonstrated the anticancer efficiency of PNP. In vivo mice experiment also suggested that the tumor accumulation and penetration of the PNP further enhanced the antitumor efficacy and reduced the common adverse effects of clinically used drugs. This work thus provides a strategy for designing a self-assembly system for autophagy inhibition to kill cancer.

Author statement

All animal experiments were performed in accordance with the guidelines of the institutional animal care and use committee (IACUC) of Westlake University.

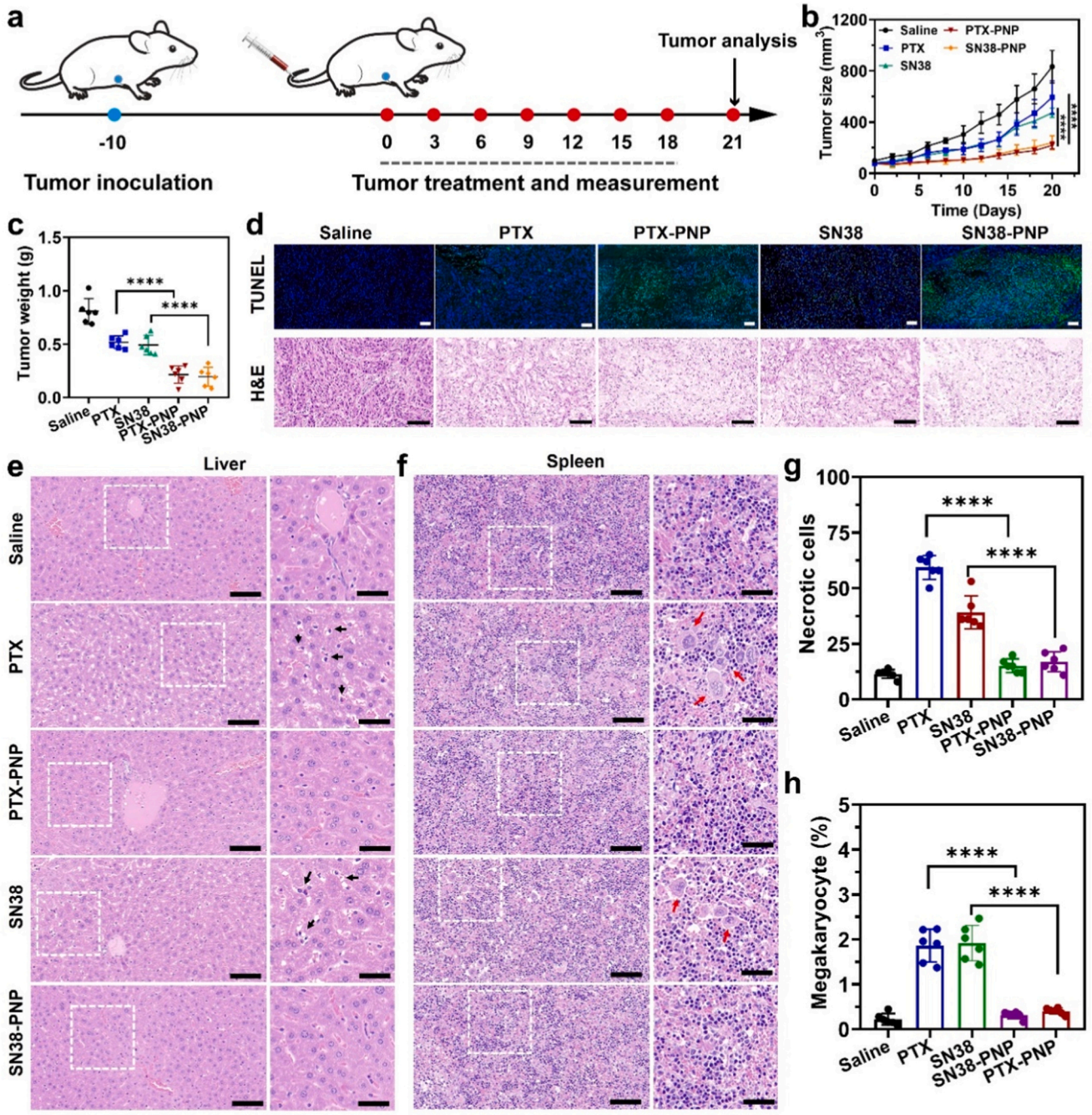

Fig. 7. Antitumor effects of **PTX-PNP** and **SN38-PNP** in vivo. (a) Schematic illustration of subcutaneous tumor inoculation, compound injection, tumor measurement, and analysis. (b) Tumor growth curves in A549 tumor-bearing mice after intravascular (i.v.) injections of saline, PTX, SN38, **PTX-PNP**, and **SN38-PNP**. The injection doses of drugs are equal to 10 mg/kg for each treatment. Data are presented as mean ± SD, n = 6, ****p < 0.0001, two-way ANOVA. (c) Weights of dissected tumors of tumor-bearing mice after treatments. Data are presented as mean ± SD, n = 6, ****p < 0.0001, one-way ANOVA. (d) H&E and TUNEL staining images of tumor tissues for each treatment. Scar bars are 20 μm. (e-f) H&E staining images of liver and spleen tissues of each group. Scar bars are 20 μm in the low-magnification images and 10 μm in the high-magnification images. (g) Statistical necrotic cells in the corresponding H&E staining images of liver tissues in g. Data are presented as mean ± SD, n = 6, ****p < 0.0001, one-way ANOVA. (h) Percentage of megakaryocyte in the corresponding H&E staining images of spleen tissues in g. Data are presented as mean ± SD, n = 6, ****p < 0.0001, one-way ANOVA.

CRediT authorship contribution statement

Jing Wang: Writing – review & editing, Writing – original draft, Methodology, Investigation, Formal analysis, Data curation. **Huaimin Wang:** Writing – review & editing, Writing – original draft, Project administration, Investigation, Funding acquisition, Formal analysis, Conceptualization. **Laicheng Zhou:** Validation, Data curation.

Declaration of Competing Interest

The authors declare that they have no known competing financial interests or personal relationships that could have appeared to influence the work reported in this paper.

Data Availability

Data will be made available on request.

Acknowledgements

This project was supported by the National Natural Science Foundation of China (82272145). We thank the Instrumentation and Service Center for Molecular Sciences, Instrumentation and Service Center for Physical Sciences, General Equipment Core Facility, Biomedical Research Core Facilities, and Laboratory Animal Resource Center at Westlake University for the assistance with measurements.

Appendix A. Supporting information

Supplementary data associated with this article can be found in the online version at doi:10.1016/j.nantod.2024.102317.

References

[1] D.J. Klionsky, Autophagy 4 (2008) 740.
[2] J.M.M. Levy, C.G. Towers, A. Thorburn, Nat. Rev. Cancer 17 (2017) 528.
[3] C.B. Lebovitz, S.B. Bortnik, S.M. Gorski, Clin. Cancer Res. 18 (2012) 1214.
[4] A. Takamura, M. Komatsu, T. Hara, A. Sakamoto, C. Kishi, S. Waguri, Y. Eishi, O. Hino, K. Tanaka, N. Mizushima, Genes Dev. 25 (2011) 795.
[5] R.K. Amaravadi, A.C. Kimmelman, J. Debnath, Cancer Discov. 9 (2019) 1167.
[6] V.J.A. Barthet, M. Brucoli, M. Ladds, C. Nössing, C. Kiourtis, A.D. Baudot, J. O'Prey, B. Zunino, M. Müller, S. May, C. Nixon, J.S. Long, T.G. Bird, K.M. Ryan, Sci. Adv. 7 (2021).
[7] S.A. Tooze, I. Dikic, Cell 167 (2016) 1433.
[8] D.J. Klionsky, Nat. Rev. Mol. Cell Biol. 8 (2007) 931.
[9] G. Xi, X. Hu, B. Wu, H. Jiang, C.Y. Young, Y. Pang, H. Yuan, Cancer Lett. 307 (2011) 141.
[10] J.F. Lin, Y.C. Lin, T.F. Tsai, H.E. Chen, K.Y. Chou, T.I. Hwang, Drug Des, Dev. Ther. 11 (2017) 1517.
[11] Y.R. Feliz-Mosquea, A.A. Christensen, A.S. Wilson, B. Westwood, J. Varagic, G. C. Meléndez, A.L. Schwartz, Q.R. Chen, L. Mathews Griner, R. Guha, C.J. Thomas, M. Ferrer, M.J. Merino, K.L. Cook, D.D. Roberts, D.R. Soto-Pantoja, Breast Cancer Res. Treat. 172 (2018) 69.
[12] Q. Cai, S. Wang, L. Jin, M. Weng, D. Zhou, J. Wang, Z. Tang, Z. Quan, Mol. Cancer 18 (2019) 82.
[13] P. Maycotte, S. Aryal, C.T. Cummings, J. Thorburn, M.J. Morgan, A. Thorburn, Autophagy 8 (2012) 200.
[14] C.H. Eng, Z. Wang, D. Tkach, L. Toral-Barza, S. Ugwonali, S. Liu, S.L. Fitzgerald, E. George, E. Frias, N. Cochran, R. De Jesus, G. McAllister, G.R. Hoffman, K. Bray, L. Lemon, J. Lucas, V.R. Fantin, R.T. Abraham, L.O. Murphy, B. Nyfeler, Proc. Natl. Acad. Sci. 113 (2016) 182.
[15] R.A. Barnard, L.A. Wittenburg, R.K. Amaravadi, D.L. Gustafson, A. Thorburn, D. H. Thamm, Autophagy 10 (2014) 1415.
[16] L.C. Palmer, S.I. Stupp, Acc. Chem. Res. 41 (2008) 1674.
[17] Z. Feng, T. Zhang, H. Wang, B. Xu, Chem. Soc. Rev. 46 (2017) 6470.
[18] J. Gao, J. Zhan, Z. Yang, Adv. Mater. 32 (2020) 1805798.
[19] J. Boekhoven, W.E. Hendriksen, G.J. Koper, R. Eelkema, J.H. van Esch, Science 349 (2015) 1075.
[20] A. Levin, T.A. Hakala, L. Schnaider, G.J. Bernardes, E. Gazit, T.P. Knowles, Nat. Rev. Chem. 4 (2020) 615.
[21] D.J. Smith, G.A. Brat, S.H. Medina, D. Tong, Y. Huang, J. Grahammer, G. J. Furtmüller, B.C. Oh, K.J. Nagy-Smith, P. Walczak, Nat. Nanotechnol. 11 (2016) 95.
[22] D. Wu, N. Sinha, J. Lee, B.P. Sutherland, N.I. Halaszynski, Y. Tian, J. Caplan, H. V. Zhang, J.G. Saven, C.J. Kloxin, Nature 574 (2019) 658.
[23] Y. Cai, H. Shen, J. Zhan, M. Lin, L. Dai, C. Ren, Y. Shi, J. Liu, J. Gao, Z. Yang, J. Am. Chem. Soc. 139 (2017) 2876.
[24] D.-B. Cheng, D. Wang, Y.-J. Gao, L. Wang, Z.-Y. Qiao, H. Wang, J. Am. Chem. Soc. 141 (2019) 4406.
[25] Y. Ding, D. Zheng, L. Xie, X. Zhang, Z. Zhang, L. Wang, Z.-W. Hu, Z. Yang, J. Am. Chem. Soc. 145 (2023) 4366.
[26] G. Gao, Y.-W. Jiang, W. Zhan, X. Liu, R. Tang, X. Sun, Y. Deng, L. Xu, G. Liang, J. Am. Chem. Soc. 144 (2022) 11897.
[27] B. Jana, S. Jin, E.M. Go, Y. Cho, D. Kim, S. Kim, S.K. Kwak, J.-H. Ryu, J. Am. Chem. Soc. 145 (2023) 18414.
[28] H. Su, F. Wang, Y. Wang, A.G. Cheetham, H. Cui, J. Am. Chem. Soc. 141 (2019) 17107.
[29] H. Su, W. Zhang, H. Wang, F. Wang, H. Cui, J. Am. Chem. Soc. 141 (2019) 11997.
[30] A. Tanaka, Y. Fukuoka, Y. Morimoto, T. Honjo, D. Koda, M. Goto, T. Maruyama, J. Am. Chem. Soc. 137 (2015) 770.
[31] R.A. Pires, Y.M. Abul-Haija, D.S. Costa, R. Novoa-Carballal, R.L. Reis, R.V. Ulijn, I. Pashkuleva, J. Am. Chem. Soc. 137 (2015) 576.
[32] M. Pieszka, S. Han, C. Volkmann, R. Graf, I. Lieberwirth, K. Landfester, D.Y. Ng, T. Weil, J. Am. Chem. Soc. 142 (2020) 15780.
[33] Z. Feng, H. Wang, S. Wang, Q. Zhang, X. Zhang, A.A. Rodal, B. Xu, J. Am. Chem. Soc. 140 (2018) 9566.
[34] Z. Feng, H. Wang, B. Xu, J. Am. Chem. Soc. 140 (2018) 16433.
[35] S. Li, Q. Zou, Y. Li, C. Yuan, R. Xing, X. Yan, J. Am. Chem. Soc. 140 (2018) 10794.
[36] X. Yang, H. Lu, Y. Tao, L. Zhou, H. Wang, Angew. Chem. 133 (2021) 23990.
[37] H. He, W. Tan, J. Guo, M. Yi, A.N. Shy, B. Xu, Chem. Rev. 9994 (2020) 120.
[38] S. Chagri, D.Y. Ng, T. Weil, Nat. Rev. Chem. 6 (2022) 320.
[39] J. Kim, S. Lee, Y. Kim, M. Choi, I. Lee, E. Kim, C.G. Yoon, K. Pu, H. Kang, J.S. Kim, Nat. Rev. Mater. 8 (2023) 710.
[40] Q. Luo, Y.-X. Lin, P.-P. Yang, Y. Wang, G.-B. Qi, Z.-Y. Qiao, B.-N. Li, K. Zhang, J.-P. Zhang, L. Wang, Nat. Commun. 9 (2018) 1802.
[41] J.R. Casey, S. Grinstein, J. Orlowski, Nat. Rev. Mol. Cell Biol. 11 (2010) 50.
[42] M.R. Sawaya, S. Sambashivan, R. Nelson, M.I. Ivanova, S.A. Sievers, M.I. Apostol, M.J. Thompson, M. Balbirnie, J.J. Wiltzius, H.T. McFarlane, Nature 447 (2007) 453.
[43] F. Wang, H. Su, D. Xu, W. Dai, W. Zhang, Z. Wang, C.F. Anderson, M. Zheng, R. Oh, F. Wan, Nat. Biomed. Eng. 4 (2020) 1090.
[44] Y. Gao, Y. Kuang, Z.-F. Guo, Z. Guo, I.J. Krauss, B. Xu, J. Am. Chem. Soc. 131 (2009) 13576.
[45] J. Zhan, Y. Cai, S. He, L. Wang, Z. Yang, Angew. Chem., Int. Ed. 57 (2018) 1813.
[46] H. Wang, Y. Song, W. Wang, N. Chen, B. Hu, X. Liu, Z. Zhang, Z. Yu, J. Am. Chem. Soc. 146 (2023) 330.
[47] Z. Zheng, P. Chen, M. Xie, C. Wu, Y. Luo, W. Wang, J. Jiang, G. Liang, J. Am. Chem. Soc. 138 (2016) 11128.
[48] G. Liang, H. Ren, J. Rao, Nat. Chem. 2 (2010) 54.
[49] L. Hu, Y. Li, X. Lin, Y. Huo, H. Zhang, H. Wang, Angew. Chem., Int. Ed. 60 (2021) 21807.
[50] H. Su, F. Wang, W. Ran, W. Zhang, W. Dai, H. Wang, C.F. Anderson, Z. Wang, C. Zheng, P. Zhang, Proc. Natl. Acad. Sci. 117 (2020) 4518.
[51] K. Umezawa, M. Yoshida, M. Kamiya, T. Yamasoba, Y. Urano, Nat. Chem. 9 (2017) 279.
[52] X. Jiang, Y. Yu, J. Chen, M. Zhao, H. Chen, X. Song, A.J. Matzuk, S.L. Carroll, X. Tan, A. Sizovs, N. Cheng, M.C. Wang, J. Wang, ACS Chem. Biol. 10 (2015) 864.
[53] Y. Gao, J. Shi, D. Yuan, B. Xu, Nat. Commun. 3 (2012) 1033.
[54] F. Wang, R. Gómez-Sintes, P. Boya, Traffic 19 (2018) 918.
[55] L. Galluzzi, J.M. Bravo-San Pedro, B. Levine, D.R. Green, G. Kroemer, Nat. Rev. Drug Discov. 16 (2017) 487.
[56] M.A. Taylor, B.C. Das, S.K. Ray, Apoptosis 23 (2018) 563.
[57] P. García-Sanz, L. Orgaz, J.M. Fuentes, C. Vicario, R. Moratalla, Autophagy 14 (2018) 717.
[58] E.J. Blanchette-Mackie, Biochim. Biophys. Acta 1486 (2000) 171.
[59] F.M. Platt, B. Boland, A.C. van der Spoel, J. Cell Biol. 199 (2012) 723.
[60] S.N. Pressey, D.A. Smith, A.M. Wong, F.M. Platt, J.D. Cooper, Neurobiol. Dis. 45 (2012) 1086.
[61] A.H. Futerman, G. van Meer, Nat. Rev. Mol. Cell Biol. 5 (2004) 554.